Available online at www.sciencedirect.com
SCIENCE DIRECT®
ELSEVIER
Ultramicroscopy 100 (2004) 429–436
ultramicroscopy
www.elsevier.com/locate/ultramic

Probing large area surface plasmon interference in thin metal films using photon scanning tunneling microscopy

A. Passian[a,*], A. Wig[a], A.L. Lereu[a,b], P.G. Evans[a], F. Meriaudeau[c], T. Thundat[a], T.L. Ferrell[a]

[a] *Oak Ridge National Laboratory, Oak Ridge, Bethel Valley Rd., Bldg. 4500 S, MS 6123, TN 37831-6219, USA*
[b] *Département de physique, Laboratoire d'optique submicronique, Université de Bourgogne, 9 Avenue Alain Savary, 21011 Dijon, France*
[c] *Université de Bourgogne, IUT du Creusot, Le2i, 71200 Le Creusot, France*

Received 11 August 2003; received in revised form 26 October 2003; accepted 18 November 2003

Abstract

The interference of surface plasmons can provide important information regarding the surface features of the hosting thin metal film. We present an investigation of the interference of optically excited surface plasmons in the Kretschmann configuration in the visible spectrum. Large area surface plasmon interference regions are generated at several wavelengths and imaged with the photon scanning tunneling microscope. Furthermore, we discuss the non-retarded dispersion relations for the surface plasmons in the probe–metal system modeled as confocal hyperboloids of revolution in the spheroidal coordinate systems.

Keywords: Surface plasmons; Interference; Scanning probe microscopy; Dispersion relation; Metal thin films

1. Introduction

The particle-wave duality of electrons, as one of the most striking quantum mechanical effects, lies behind many intriguing phenomena of modern physics. The interference fringes recorded on a phosphorus screen as a result of passing individual electrons through a double slit arrangement in vacuum is a fundamental observation. On the other hand, in condensed matter, the complicated interaction between large numbers of electrons gives rise to the so-called collective electronic effects and is formulated as a subclass of the many body theory. For example in a noble metal such as gold, the electrons, initially in a state of equilibrium can undergo large collective oscillations in form of a propagating wave under the influence of external disturbances [1]. When two or several such electron density waves or plasmons meet, interference may occur. Ritchie [2] showed theoretically in 1957 that, at the bounding surfaces of a metal, for example at the two surfaces of a thin metal film, there exist new modes of collective electron oscillations with energies different from those electrons in the bulk of the metal. Beside being a fundamental concept, these new modes called surface plasmons found many important applications due to their contribution to surface

*Corresponding author. +1-865-574-6219; fax: +1-865-574-6210.
E-mail address: passian@utk.edu (A. Passian).

0304-3991/$ - see front matter © 2004 Elsevier B.V. All rights reserved.
doi:10.1016/j.ultramic.2003.11.018

sensitivity and field enhancement [3–19]. Strictly speaking, a surface plasmon is a quantum of the surface electron density wave, much in the same way as a photon is a quantum of the electromagnetic waves. The aim of this article is to study the interference of surface plasmons in thin metal films and, using scanning probe microscopy (SPM), image the resulting fringes over large areas of the film.

Optical excitation of surface plasmons in metals is typically accomplished by placing a thin layer of a metal such as gold on a dielectric substrate. One then disturbs the electronic equilibrium of the gold film by exposing it to the oscillating electric field of a laser beam incident from the dielectric side. Apart from being practical, this arrangement, called the Kretschmann configuration [20], provides the necessary conditions for optically stimulating the surface electron density waves. Utilizing the Kretschmann configuration in this work, in order to arrange for the interference of surface plasmons, we present two different beam geometries heretofore referred to as the single- and the split-beam geometries.

The electron oscillations being characterized by a wave may, under proper conditions, result in a standing wave in the film plane and thus the electron density may display periodic modulation. One would then expect this modulation to be measurable via the tunneling of the node electrons (as opposed to anti-node) into the metallic probe of a scanning tunneling microscope (STM) [21] or the tunneling of photons associated with their electromagnetic field into the dielectric probe of a photon scanning tunneling microscope (PSTM) [22]. In this work, we demonstrate this effect by using the latter. The principle of the operation of the PSTM is photon tunneling between two optically conductive media. The probe composes one of the media, while the surface under study belongs to the second. Local surface plasmon scattering and interference have been studied in various SPM experiments such as in scanning near field optical microscopy (SNOM) [23,24], or in PSTM [25,26] to mention a few. Here, we present an explicit method to generate standing surface plasmons over any region of the metal film and image the resulting fringes without perturbing

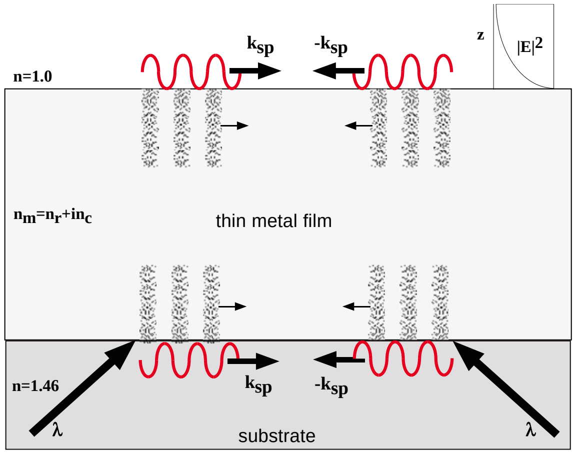

Fig. 1. Schematic representation of surface plasmon generation and propagation in a thin metal film. Two coherent optical fields of wavelength λ will generate two counter propagating surface plasmons of wave vector k_{sp} which may under proper conditions interfere.

their characteristics. This is schematically shown in Fig. 1. The interference of surface plasmons is formulated in Section 2, while the experimental arrangements are shown in Section 3. The results are discussed in Section 4, with a conclusion given in Section 5.

2. Plasmon interference

In the general case of interference of two waves $\psi_m = \psi_m^0 \exp(ikr_m)$, $m = 1, 2$ in the same medium, we have the following amplitude for the superposition:

$$|\psi_1 + \psi_2|^2 = \psi_1\psi_1^* + \psi_2\psi_2^* + 2|\psi_1||\psi_2| \cos k(r_1 - r_2) \tag{1}$$

resulting in a relative contrast C between the maximum and minimum intensities

$$C = \frac{2\psi_1^0\psi_2^0}{\psi_1\psi_1^* + \psi_2\psi_2^*}. \tag{2}$$

Scattering events, in particular the inelastic kind, degrade the coherence which then may increase the constant background. These scatterers may be imperfections, impurities, and roughness related processes which could lead to

$$|\psi_1 + \psi_2|^2 \to |\psi_1|^2 + |\psi_2|^2. \quad (3)$$

In our case, we note that since the divergence of the electric field throughout the system shown in Fig. 1 is only non-zero at the interfaces (xy plane), the excited charge density ρ at the film surface ($z = 0$) is given by

$$4\pi\rho(x, z, t) = \kappa\delta(z)\psi^0(z)e^{i(\omega t - \kappa x + \pi/2)}, \quad (4)$$

accompanied by the field

$$\psi(x, z, t) = \psi^0(z)e^{i(\omega t - \kappa x)}, \quad (5)$$

where κ is the surface plasmon wave vector, which in the general case for a known excitation frequency ω, can be obtained from the retarded dispersion relation for a thin film of thickness d given by the following transcendental equation:

$$\varepsilon^2(\omega) + i\cot(k_1 d)\left(\frac{1}{k_2} + \frac{\varepsilon_0}{k_0}\right)k_1\varepsilon(\omega) + \varepsilon_0\frac{k_1^2}{k_0 k_2} = 0, \quad (6)$$

where

$$k_i(\omega) = \sqrt{\kappa^2 - \varepsilon_i(\omega)\frac{\omega^2}{c^2}} \quad (7)$$

with $\varepsilon_0 = \varepsilon_q$, $\varepsilon_1 = \varepsilon(\omega)$, and $\varepsilon_2 = 1$ while ε_q is the dielectric function of the quartz substrate. In the case of Eq. (4), however, we need the real part of the wave vector, which is just the in-plane component of the momentum of the incident photon field, i.e., $\kappa = \omega\sqrt{\varepsilon_q}\sin\theta_{sp}c^{-1}$, where θ_{sp} is the angle of incidence at which the dispersion relation of photons inside the substrate coincide with that of the surface plasmons. Thus, if we represent one of the two surface plasmon modes by

$$\psi_1(x, z, t) = \psi_1^0(z)e^{i(\omega t - \kappa x)}, \quad (8)$$

so that, as shown schematically in Fig. 1, the other can be obtained by $\kappa \to -\kappa$, i.e.,

$$\psi_2(x, z, t) = \psi_2^0(z)e^{i(\omega t + \kappa x)}, \quad (9)$$

then since in our case $\psi_1^0 \approx \psi_2^0 = \psi_0$, we get for the amplitude of the interference

$$|\psi_1 + \psi_2|^2 = 2|\psi_0|^2\left[1 + \cos\left(\frac{4\pi\sqrt{\varepsilon_q}\sin\theta_{sp}}{\lambda}\right)x\right]. \quad (10)$$

Thus, the fringes are separated by

$$\Delta x = \frac{\lambda}{2\sqrt{\varepsilon_q}\sin\theta_{sp}}, \quad (11)$$

and are distributed along the interface at locations $x_m = m\Delta x$, $m = 0, \pm 2, \pm 4, \cdots$.

3. Experimental arrangements

Following the standard realization of the Kretschmann configuration, we vacuum evaporated a spectrally optimized thickness of the selected metal (for example, 55 nm for gold at $\lambda = 632.8$ nm) onto one side of a cleaned quartz slide, while the other side was optically attached to a quartz prism using a refractive index matching gel. This arrangement was then side mounted on a rotation stage positioned on a vibration suppressed optical table so that a normal to the film was parallel to the table. The PSTM head was similarly side mounted on a mechanical arm terminated at the axis of the rotation stage such that the head and the prism-film assembly could rotate with respect to the laser beam as one unit. Using a standard sequence of coarse and fine mechanical and piezo translational and tilt controls, the probe was then placed a few hundred nanometers away from the surface of the gold. The most common form of the PSTM probe is a multimode-fused silica optical fiber with a core diameter of 50 μm which is pulled in a controlled manner using a fiber pulling device to form a sharp end.

The polarization controlled outputs of a series of He–Ne lasers and a He–Cd laser were used to excite the plasmons in the metal film at different wavelengths. The optical beam delivery system determines the type of the prism used in our experiments. The split-beam geometry shown in

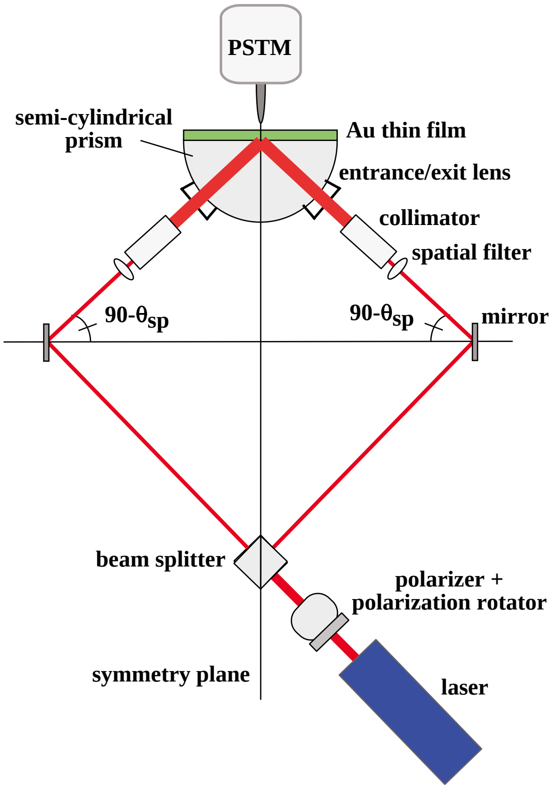

Fig. 2. The split-beam arrangement. The beam is split and the two resultants are steered to the same region of the film at the plasmon angle θ_{sp} and consequently the possible interference of the excited plasmons may be observed by the PSTM.

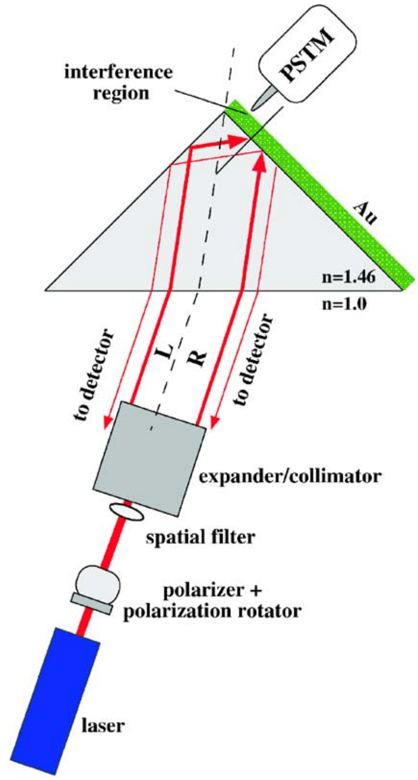

Fig. 3. The single-beam arrangement. By translating the prism along its hypotenuse, a proper portion of the beam (L) is brought into total internal reflection at the prism–air interface perpendicular to the film. This portion is thus delivered at the plasmon angle to a region of the film which is exposed by the directly delivered portion of the beam (R). The two portions excite the surface plasmons which may then undergo interference such that the resulting fringes could be detected by the PSTM probe. Condition: for the metal film used, the difference between the plasmon resonance angle and the total internal reflection critical angle is not larger than a predetermined value.

Fig. 2 uses a semi-cylindrical prism, whereas the single-beam geometry shown in Fig. 3 utilizes a right-angled prism. The advantage of the former is the ease of manipulation of the properties of the excitation beams prior to delivery appropriate for example for surface plasmon holography [27–29]. The latter requires fewer optical components as the beam is split internally by the prism itself, and thereby less risk for any possible sources of noise. In both cases, a state of polarization is selected by the polarization rotator for the laser beam which is then spatially filtered and collimated with a flexible diameter. The filtering step is essential for the generation of as uniformly excited a region as possible.

In Fig. 2, an iteration between incrementing the incidence angle and incrementing the location of the excitation region on the film allowed us to have two overlapping excitation regions. It is essential here to be at the peak plasmon angle for both beams so as to gain a high contrast in the fringes (large C). This concern becomes irrelevant in the single-beam arrangement of Fig. 3. However, when utilizing this configuration, we make the geometric observation that for the right-angled prism used, the difference between the critical angle for the total internal reflection at the prism–air interface and that of the plasmon has to be limited. For example, it is impossible to use the triangular prism for the interference experiment at He–Cd lines with an absorption peak at 60° (442 nm line, and for the same film thickness, 65° for 325 nm line). This is due to the fact that, the critical angle for the prism–air system is $\theta_c = 43.2$ and thus any plasmon angle (at peak absorption) larger than $90.0 - 43.2° = 46.8°$ will couple out and will not be totally internally reflected. Therefore, if the R-beam is at the plasmon angle θ_{sp}, the L-beam will not make it back to the R-beam spot for the interference to take place. The reason why it works with $\lambda = 632.8$ nm and higher is the fact that for these wavelengths the peak plasmon angle is less than 46.8° (46° for $\lambda = 632.8$ nm and even less for higher wavelengths) and thus half of the beam will get totally internally reflected from the non-film side of the prism. One could then attempt to stay below the peak plasmon angle for $\lambda = 442$ nm (below 46.6°) with the cost of less signal magnitude for the PSTM.

4. Results and discussions

We first note that for the used quartz prisms with an index of refraction $\sqrt{\varepsilon_q} = 1.46$, and an incident p-polarized photon field with a wavelength $\lambda = 632.8$ nm, the optimum film thickness is obtained by a simulation of optical absorption in gold to be $d = 55$ nm using experimentally determined dielectric function tabulated by Palik and Ghosh [30]. The surface plasmon resonance peak then occurs at $\theta_{sp} = 46°$, and thus by Eq. (11) we expect a fringe separation of $\Delta x = 302$ nm, approximately 14 nm below half of the excitation wavelength.

When imaging the fringes, one could question whether or not the charge density in Eq. (4) is altered as a result of the presence of the dielectric probe of the involved SPM. This can be studied by looking at the dispersion relation of the composite probe–film system. The retarded and non-retarded dispersion relations of the system in the absence of the PSTM dielectric probe, given by Eq. (6), are shown in Fig. 4. The question as to whether the loci shown in Fig. 4 are varied as a result of the approach of the tip can be addressed in the non-retarded limit. In order to include the effect of the probe dielectric, we have carried out a calculation of the non-retarded modes of the probe–film system in the spheroidal coordinate system assuming spatially local dielectric functions [31]. The probe modeled as a single sheeted hyperboloid located above a planar film is shown in Fig. 5. In short, since the system is neutral as a whole, we solve Laplace's equation subject to the continuity of the scalar electric potential, and the normal component of the displacement field everywhere. It can then be shown that the resonance values of the dielectric function of the metal undergo only negligible shifts in the long wavelength region as a result of the presence of the probe within a distance less than a wavelength of the excitation beam [31].

We now proceed to present the image of the standing plasmon wave in gold in Fig. 6 obtained by the single-beam geometry shown in Fig. 3. By operating the PSTM in the constant current mode, the image in Fig. 6 displays the result of a $6\lambda \times 6\lambda$ scan size inside the interference region at a scan rate of 2 Hz. A series of images with increasing scan size up to $12\lambda \times 12\lambda$ (7.5×7.5 μm) were obtained to observe the integrity of the fringes. From these images, we determined an average

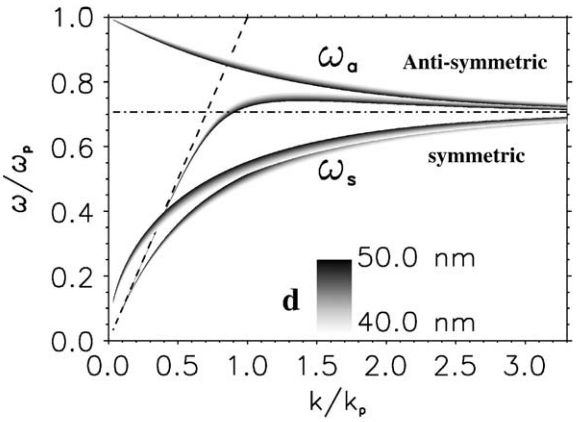

Fig. 4. Retarded and non-retarded dispersion relations of a thin gold film on a quartz substrate. The gray scale displays the variation in film thickness d. The dashed line represents the dispersion relation of photons in vacuum. The modes extending to the left of the dashed line are non-retarded, while the modes tangential to the photon line in the long wavelength region are the retarded ones.

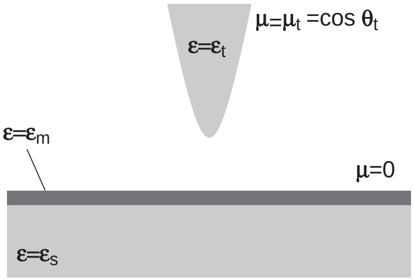

Fig. 5. Modeling the dielectric probe of the PSTM with a dielectric function ε_t above a metallic film with a dielectric function ε_m in the spheroidal system. The boundary of the probe is defined by fixing the coordinate θ_t while that of the film is given by $\theta = \pi/2$.

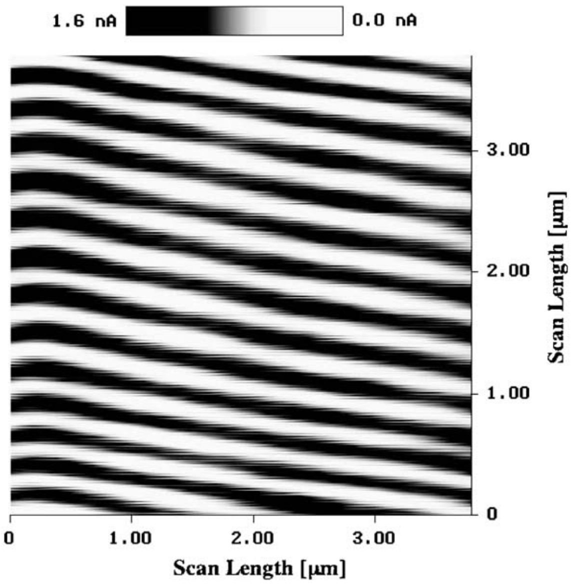

Fig. 6. Recorded standing surface plasmons excited at $\lambda = 632.8$ nm, and extended over a $6\lambda \times 6\lambda$ region. The color bar displays the relative variation in the detected current. The fringe separation can be measured to be 298 nm.

period of 298 nm for the fringes circa 4 nm less than the above-mentioned predicted value of $\Delta x = 302$ nm. This slight deviation could be attributed to the calibration of the piezo tube of the scanner.

It is worth noting here that the acquired optical signal by the probe as detected by the photomultiplier is a direct consequence of the plasmon field detection. In particular, referring to Fig. 7 we discern this signal from the traditional PSTM signal, shown in Fig. 8, where the tunneling photons are provided by the evanescent field produced by the total internal reflection at the sample/substrate interface. The experimentally detected plasmon field shown in Fig. 9 compares well with the simulated-tunneled field in Fig. 7b. They both decay within a wavelength of the exciting photons, noting that in the case of Fig. 9, the probe is located an unknown distance

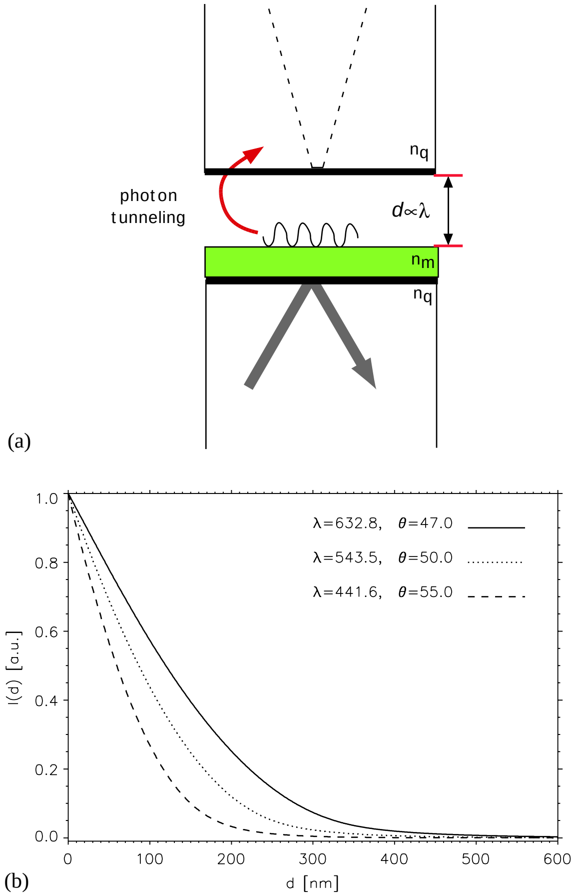

Fig. 7. Photon tunneling from the surface plasmon field set up by the resonant absorption of the metal film. (a) The dashed line depicts the boundary of the probe. (b) Simulation of the tunneled photons from the plasmon field into the dashed cone representing the probe. As can be seen for the three different wavelengths examined in this work, the shorter wavelength has a faster decay.

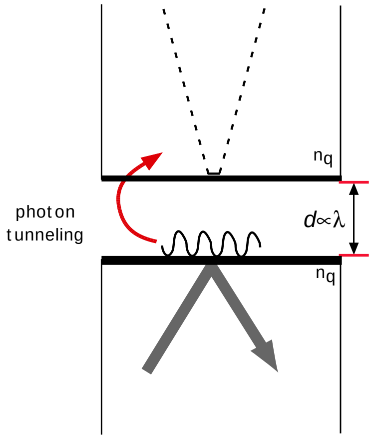

(a)

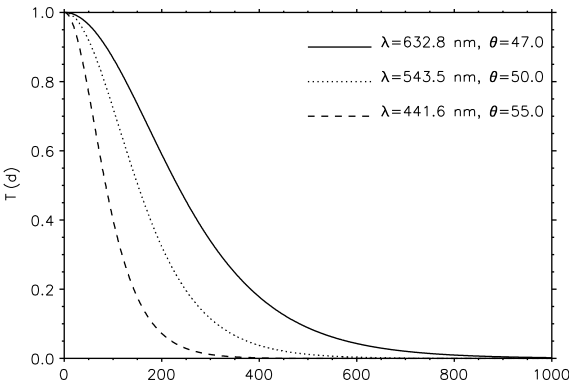

(b)

Fig. 8. Photon tunneling from the evanescent field set up by the total internal reflection of the incident field in the substrate/sample medium. (a) The dashed line depicts the boundary of the probe. (b) Simulation of the transmitted photons from the substrate into the dashed cone representing the probe. As can be seen for the three different wavelengths examined in this work, the shorter wavelength has a faster decay.

(approximately 100 nm) above the surface prior to engaging the vertical scan. The exponential behavior of the plasmon field is evident from the fitted function shown in Fig. 9, clearing any possibilities of detection of scattered light.

The occurrence of the interference fringes as a result of the standing surface plasmons at the metal surface is further supported by the deterioration/extinction of fringes ($C \to 0$) upon (a) a continuous variation of the polarization state of the incident field from $p \to s$, (b) an inhibition of either L or R beam, and (c) a shift away from resonance of the angular or spectral position of the excitation beam.

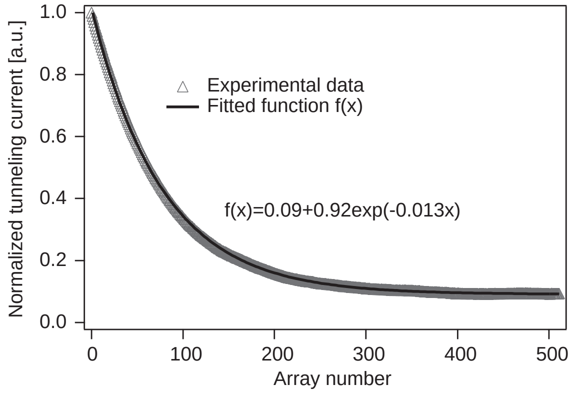

Fig. 9. The experimentally observed surface plasmon-supported photon tunneling. The solid curve represents the fitted exponential function shown in the inset. The vertical distance represented by the array numbers is such that $z(0) = z_i$ yields the absolute initial distance (unknown) and $z(512) = z_i + 1$ μm.

5. Conclusions

We have presented a straightforward method for generating and imaging standing surface plasmons in thin metal films. When imaging the field of the plasmons, the presence of the dielectric probe has negligible effect on the modes of the substrate metal surface. From our results we conclude that plasmon interference can be sustained in arbitrarily large regions in comparison to the excitation wavelength. This knowledge can be important when evaluating the smoothness of the film surface or seeking the relative distance between two scattering centers such as the presence of micron or sub-micron structures. In particular, the potential of such information for detection of scattering centers can be used in single molecule detection techniques on metal surfaces. Our experimental configurations can be appropriate for surface plasmon holography, while access to film surface is beneficial for sensing applications. Variations in physical quantities such as temperature, volume, and elasticity that cause either of the two interfering beam phase or amplitude variations may be detected using the presented method.

Acknowledgements

This work was supported by the DOE Office of Biological and Environmental Research (OBER). Oak Ridge National Laboratory, Oak Ridge, Tennessee, 37831-6123, is managed by UT-Battelle, LLC for the Department of Energy under contract number DE-AC05-0096OR22725.

References

[1] T.L. Ferrell, T.A. Callcott, R.J. Warmack, Am. Sci. 73 (1985) 344.
[2] R.H. Ritchie, Phys. Rev. 106 (1957) 874.
[3] P. Englebienne, A. Van Hoonacker, M. Verhas, Spectroscopy: An International Journal 17 (2/3) (2003) 255.
[4] F. Meriaudeau, T.R. Downey, A. Passian, A. Wig, T.L. Ferrell, Appl. Opt. 37 (1998) 34.
[5] W.H. Weber, G.W. Ford, Opt. Lett. 6 (1981) 122.
[6] F. Meriaudeau, T.R. Downey, A. Wig, A. Passian, M. Buncick, T.L. Ferrell, Sensor Actuator B 54 (1999) 106.
[7] M.E. Caldwell, E.M. Yeatman, Appl. Opt. 31 (1992) 3880.
[8] J. Homola, S.S. Yee, G. Gauglitz, Sensor Actuator B 54 (1999) 3.
[9] M. Mehrvar, C. Bis, J.M. Scharer, M. Moo-Young, J.H. Luong, Anal. Sci. 16 (2000) 677.
[10] S. Hayashi, K. Kozaru, K. Yamamoto, Solid State Commun. 79 (1991) 763.
[11] C. Nylander, B. Liedberg, T. Lind, Sensor Actuator 3 (1982/1983) 79.
[12] K. Matsubara, S. Kawata, S. Minami, Appl. Opt. 27 (1988) 1160.
[13] W. Hickel, B. Rothenhausler, W. Knoll, J. Appl. Phys. 66 (1989) 4832.
[14] F. Meriaudeau, A. Wig, A. Passian, T. Downey, M. Buncick, T.L. Ferrell, Sensor Actuator B 69 (2000) 51.
[15] T. Okamoto, I. Yamaguchi, Opt. Commun. 93 (1992) 265.
[16] H. Kano, S. Kawata, Appl. Opt. 33 (1994) 5166.
[17] R.T. Deck, D. Sarid, J. Opt. Soc. Am. 72 (1982) 1613.
[18] R.E. Benner, R. Dornhaus, R.K. Chang, Opt. Commun. 30 (1979) 145.
[19] J.W. Attridge, P.B. Daniels, J.K. Deacon, G.A. Robinson, G.P. Davidson, Biosens. Bioelectron. 6 (1991) 201.
[20] E. Kretschmann, Z. Phys. 241 (1971) 313.
[21] G. Binnig, H. Rohrer, Helv. Phys. Acta. 55 (1982) 726.
[22] R.C. Reddick, R.J. Warmack, T.L. Ferrell, Phys. Rev. B 39 (1989) 767.
[23] L. Novotny, H. Hecht, D.W. Pohl, J. Appl. Phys. 81 (4) (1997) 1798.
[24] A. Bouhelier, T. Huser, H. Tamaru, H.-J. Guntherodt, D.W. Pohl, F.I. Baida, D. Van Labeke, Phys. Rev. B 63 (2001) 155404.
[25] J.R. Krenn, J.C. Weeber, A. Dereux, E. Bourillot, J.P. Goudonnet, B. Schider, A. Leitner, F.R. Aussenegg, C. Girard, Phys. Rev. B 60 (1999) 5029.
[26] J.C. Weeber, J.R. Krenn, A. Dereux, B. Lamprecht, Y. Lacroute, P. Goudonnet, Phys. Rev. B 64 (2001) 045411.
[27] J.J. Cowan, AIP Conference Proceedings, Vol. 65, 1980, pp. 515.
[28] J.J. Cowan, in: J.P. Ebbeni, M. Monfils, (Eds.), Three-Dimensional Imaging, Proceedings of SPIE, Vol. 402, 1983, pp. 25.
[29] J.J. Cowan, in: C. Outwater, (Ed.), Optics in Entertainment II, Proceedings of SPIE, Vol. 462, 1984, pp. 20.
[30] E.D. Palik, G. Ghosh, Electronic Handbook of Optical Constants of Solids, Academic Press, San Diego, 1999.
[31] A. Passian, T. Thundat, T.L. Ferrell, preprint.